Deformation of the proton emitter ^{113}Cs from electromagnetic transition and proton-emission rates

D. Hodge,[1] D. M. Cullen,[1] M. J. Taylor,[1,*] B. S. Nara Singh,[1] L. S. Ferreira,[2] E. Maglione,[3] J. F. Smith,[4] C. Scholey,[5]
P. Rahkila,[5] T. Grahn,[5] T. Braunroth,[6] H. Badran,[5] L. Capponi,[4] A. Girka,[5] P. T. Greenlees,[5] R. Julin,[5] J. Konki,[5]
M. Mallaburn,[1] O. Nefodov,[5] G. G. O'Neill,[7] J. Pakarinen,[5] P. Papadakis,[5] J. Partanen,[5] P. Ruotsalainen,[5] M. Sandzelius,[5]
J. Sarén,[5] M. Smolen,[4] J. Sorri,[5] S. Stolze,[5] and J. Uusitalo[5]

[1]*School of Physics and Astronomy, Schuster Building, The University of Manchester, Manchester M13 9PL, United Kingdom*
[2]*Centro de Física e Engenharia de Materiais CeFEMA and Departamento de Física, Instituto Superior Técnico, Universidade de Lisboa,
Av Rovisco Pais, 1049 001, Lisboa, Portugal*
[3]*Dipartimento di Fisica e Astronomia "G. Galilei" Via Marzolo 8, I-35131, Padova, Italy and Istituto Nazionale di Fisica Nucleare,
I-35131, Padova, Italy*
[4]*School of Engineering and Computing, University of the West of Scotland, Paisley PA1 2BE, United Kingdom*
[5]*University of Jyvaskyla, Department of Physics, P.O. Box 35, Jyvaskyla FI-40014, Finland*
[6]*Institut für Kernphysik, Universität zu Köln, D-50937 Köln, Germany*
[7]*Department of Physics, Oliver Lodge Laboratory, University of Liverpool, Liverpool L69 7ZE, United Kingdom*

The lifetime of the $(11/2^+)$ state in the band above the proton-emitting $(3/2^+)$ state in ^{113}Cs has been measured to be $\tau = 24(6)$ ps from a recoil-decay-tagged differential-plunger experiment. The measured lifetime was used to deduce the deformation of the states using wave functions from a nonadiabatic quasiparticle model to independently calculate both proton-emission and electromagnetic γ-ray transition rates as a function of deformation. The only quadrupole deformation, which was able to reproduce the experimental excitation energies of the states, the electromagnetic decay rate of the $(11/2^+)$ state and the proton-emission rate of the $(3/2^+)$ state, was found to be $\beta_2 = 0.22(6)$. This deformation is in agreement with the earlier proton emission studies which concluded that ^{113}Cs was best described as a deformed proton emitter, however, it is now more firmly supported by the present measurement of the electromagnetic transition rate.

I. INTRODUCTION

Proton emission can provide valuable nuclear-structure information and allow sensitive tests of theoretical nuclear models for proton-rich nuclei in the region beyond the drip line [1,2]. Advances in experimental techniques [3,4] and the associated new experimental data can allow extensions to these models to be made [5,6], especially those models which explore the coupling of weakly bound and unbound states to the continuum. Proton emission from ^{113}Cs was first discovered in 1984 by Faestermann *et al.* [7]. In that work and others [7–10], the cross section of ^{113}Cs was established to be ~ 30 μb in the ^{58}Ni(^{58}Ni, $p2n$) reaction at 230 MeV. The $(3/2^+)$ ground state of ^{113}Cs is now established to decay with the emission of a single 969(8)-keV proton with a half-life of 17.1(2) μs [11].

Several theoretical studies have been performed to explain proton emission from nuclei. Many of these studies have considered the proton tunneling through a spherical nuclear potential within various models (for example, the Wentzel-Kramers-Brillouin (WKB), two-potential, and distorted wave

Born approaches [12,13]). Although these early approaches were found to work well for nuclei near to the spherical closed shells, for other nuclei, like ^{113}Cs, the calculated proton-transition rates failed to match the experimental half-lives of the proton-emitting ground state. For example in the spherical WKB calculations of Åberg *et al.* [12,13], proton emission from the $d_{5/2}$ state in ^{113}Cs was predicted to have a half-life of ~ 0.5 μs, which became ~ 0.9 μs when the $d_{5/2}$ state spectroscopic factor was included. This remains a factor of ~ 19 times shorter than the established 17.1(2)-μs experimental half-life [7–11]. Already, more than 25 years ago, it was suggested that the absence of deformation in these models may explain the discrepancies [14]. In an attempt to alleviate these problems, Bugrov and Kadmensky included configuration-mixing effects associated with deformation into their calculations for ^{113}Cs [14]. Proton-emission half-lives were calculated as a function of quadrupole deformation for the $d_{5/2}$, $g_{7/2}$, $g_{9/2}$ (extruder) or $h_{11/2}$ (intruder) orbits that were predicted to be occupied by the odd proton above the $Z = 50$ closed shell [14]. With these spherical configuration-mixed calculations, agreement with the 17.1(2)-μs experimental proton emission half-life was only found for a $K^\pi = 3/2^+$ orbital at a quadrupole deformation, $\beta_2 = 0.2$. In 1995, Möller and Nix performed a series of global deformation calculations using a finite-range droplet macroscopic and folded-Yukawa single-particle microscopic model [15]. The results of these microscopic calculations turned out to be in agreement with the earlier spherical configuration-mixed calculations of Bugrov *et al.* [14] and predicted that ^{113}Cs most likely had a deformation of $\beta_2 = 0.21$. The first attempt to fully account for proton emission in a deformed potential

was performed for ^{113}Cs in 1998 by Maglione *et al.* [16]. In that work, the absolute decay width of a single-particle level in a deformed Woods-Saxon potential was calculated which, for the first time, allowed the underlying nature of the $3/2^+$ proton-emitting state to be more fully evaluated as a function of deformation in ^{113}Cs [16]. The correct experimental decay width for proton emission in ^{113}Cs was reproduced with a quadrupole deformation $\beta_2 = 0.15$–0.20 [16]. Further developments of that work allowed improved wave functions to be obtained using a nonadiabatic quasiparticle model [17–19]. These nonadiabatic calculations have been used for ^{113}Cs in the present work to allow for any non rigid-rotational components in the daughter nucleus, ^{112}Xe.

In order to validate the theoretical predictions of deformation in these nuclei, any experimental information on the deformation of the proton-emitting states in ^{113}Cs, or even the states in the bands built upon them, is necessary. To date, three separate recoil-decay tagging experiments have been performed to study ^{113}Cs at Oak Ridge and Argonne National Laboratories [20] and more recently at the University of Jyväskylä [11]. In the latter recoil-decay tagging experiment, the level scheme above the proton emitting state in ^{113}Cs was more firmly assigned [11]. From the aligned angular momentum behavior, observed band crossings and blocking arguments, a rotational band, band 1, was assigned to be based upon a $g_{7/2}$ [422]3/2 configuration and a second band, band 2, upon a $d_{5/2}$ [420]1/2 configuration. In the present work, the lifetime of the $(11/2^+)$ state in band 1 has been measured using a differential-plunger device [3]. The lifetime has been interpreted within a new theoretical framework which considers both electromagnetic transition and proton emission rates using a common deformation and a common set of wave functions from a nonadiabatic quasiparticle model [17–19]. This approach has demonstrated that ^{113}Cs is best described as a deformed nucleus with a quadrupole deformation parameter, $\beta_2 = 0.22(6)$.

II. EXPERIMENTAL DETAILS

The ^{58}Ni(^{58}Ni, $p2n$) reaction was used for 12 days to populate excited states in ^{113}Cs. A 230-MeV, 4-pnA ^{58}Ni beam was provided by the University of Jyväskylä K130 cyclotron. This beam was directed onto a 1.1 mg/cm^2 ^{58}Ni target foil, which was mounted in the differential plunger for unbound states (DPUNS) [3] along with a downstream, 1.5 mg/cm^2 Mg degrader foil. Nuclei recoiling from the target foil, traveling with a velocity measured to be $v/c = 0.038(2)$, were slowed by the degrader foil to a velocity of $v/c = 0.018(2)$. The two resultant Doppler-shifts split the intensity of each γ-ray transition into respective fully shifted, I_s, and degraded, I_d, components. This allowed the implementation of the differential decay curve method (DDCM) within the recoil distance Doppler-shift (RDDS) technique [4,21].

The JUROGAM-II array of 39 Compton-suppressed germanium detectors surrounded the differential plunger at the target position [22–24]. The germanium detectors were arranged into four distinct "rings" with angles of $\theta = 76°$, $105°$, $134°$, and $158°$ with respect to the beam axis. Ten EUROGAM Phase I-type detectors situated at $\theta = 134°$ are

collectively referred to as Ring 2. This ring of detectors had an absolute efficiency of $\sim 1.0\%$ at 1.3 MeV and was found to be the only detector ring with sufficient statistics and a sufficiently large detection angle to resolve both the ^{113}Cs fully shifted- and degraded-peak components of the transitions used in the RDDS analysis (see later).

After passing through the degrader foil, the recoiling nuclei were transmitted through the gas-filled recoil ion transport unit (RITU) [25], triggering a multiwire proportional counter (MWPC) before implanting into one of the two double-sided silicon strip detectors (DSSD) of the GREAT spectrometer [26]. The average DSSD rate was ~ 9.5 kHz throughout the experiment. All detector signals were time stamped by the total data readout (TDR) system [27] and the data were sorted with the grain software package [28]. In this work, recoil-tagged events were created by imposing conditions on the energy loss of the recoils in the MWPC and the time-of-flight between the MWPC and pair of DSSDs. These conditions allowed the separation of recoil events from any scattered- or primary-beam background in the DSSDs. Recoil-decay tagging (RDT) [29] was used to correlate prompt γ rays detected in JUROGAM-II with proton decays of ^{113}Cs detected up to ~ 12 half-lives (~ 0.2 ms) after a recoil implant in the same DSSD pixel. In order to distinguish between recoil-decay events and recoil implants from subsequent beam pulses in the same DSSD pixel, recoil-decay events were identified by their detection in anti-coincidence with the MWPC signal. Figure 1(a) shows a two-dimensional spectrum of time after recoil implant versus DSSD energy for these decay events.
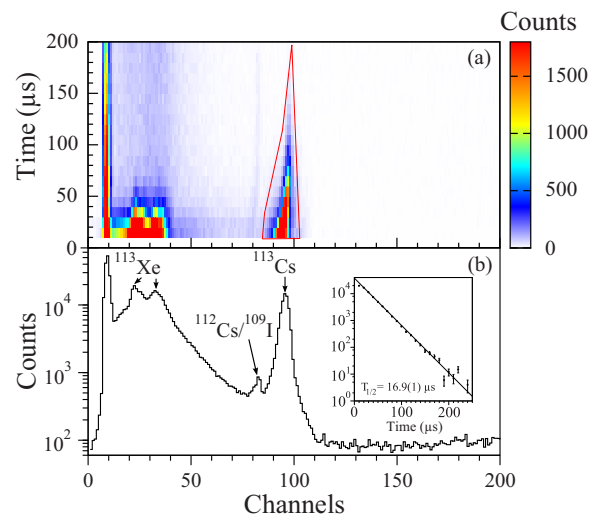

FIG. 1. (a) Two-dimensional histogram of DSSD energy versus time for decay events in anticoincidence with an MWPC signal. The area contained within the red line in (a) was used as the two-dimensional RDT gate for ^{113}Cs in this work. (b) The one-dimensional total energy projection of the two-dimensional histogram. Proton decays are identified from ^{113}Cs [11], ^{109}I (813(4)-keV, $T_{1/2} \sim 100\,\mu$s [31]), ^{112}Cs (807(7)-keV, $T_{1/2} \sim 500\,\mu$s [30]) and internal conversion electrons from the $T_{1/2} = 6.9(3)-\mu$s isomer decay in ^{113}Xe [32]. The inset to (b) shows the number of events within the ^{113}Cs two-dimensional RDT gate as a function of time, demonstrating the 16.9(1) μs ^{113}Cs proton-decay half-life.

The decay events corresponding to the proton emission from ^{113}Cs are enclosed by the red two-dimensional RDT gate shown in Fig. 1(a). This subset of events covered a proton energy range of 850–1030 keV and time difference range between 10–200 μs, overlapping the established ^{113}Cs proton decay properties [11]. This two-dimensional gate was used to construct the proton-tagged RDT spectra for the RDDS analysis in this work. Figure 1(b) is an energy projection of this matrix which shows proton decays from ^{113}Cs [11] (from the $p2n$ reaction exit channel), ^{109}I (from the $\alpha p2n$ reaction exit channel), ^{112}Cs (from the $p3n$ reaction exit channel) [30,31], and internal conversion electrons from the 6.9(3)-μs isomer decay half-life in ^{113}Xe [32]. Note that within the energy resolution of the DSSD detector, the 813(4)-keV proton-decay energy of ^{109}I [31] overlaps with the 807(7)-keV proton-decay energy of ^{112}Cs [30]. However, the proton decay half-life is dominated by the more intensely produced ^{109}I ($T_{1/2} \sim 100~\mu$s) compared with the more weakly produced ^{112}Cs ($T_{1/2} \sim 500~\mu$s) [11]. The inset to Fig. 1(b) shows the 16.9(1)-μs proton-decay half-life extracted for the proton decay of ^{113}Cs from the present data. This value is consistent with the previously accepted value 17.1(2) μs from Ref. [11].

III. RESULTS

A partial level scheme for ^{113}Cs is shown in Fig. 2 from Ref. [11]. This figure highlights the low-lying levels of the two previously identified bands 1 and 2 which are relevant to the present work. RDDS lifetime analysis was performed on the 384-keV, $(11/2^+)$ to $(7/2^+)$ transition in band 1. The 384-keV transition proved to be the only transition in the proton-tagged γ-ray spectra which had sufficient statistics and separation from other transitions to allow a full DDCM analysis to be
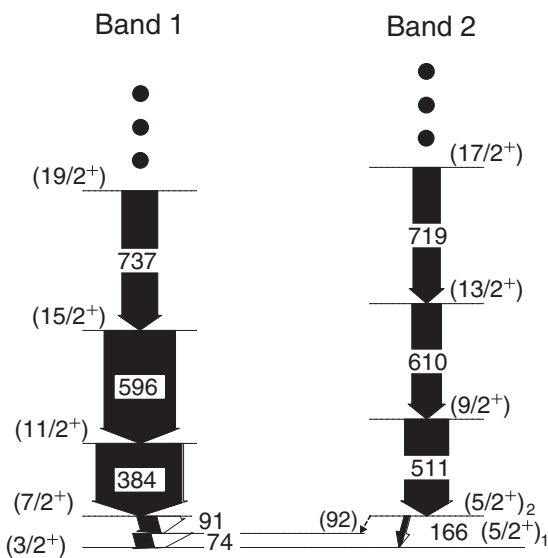

FIG. 2. A partial level scheme of ^{113}Cs showing the lower energy states of rotational bands 1 and 2 [11]. The width of each γ-ray transition arrow represents its relative intensity with the white part representing the internal-conversion component. The RDDS analysis was performed using the 384-keV, $(11/2^+)$ to $(7/2^+)$ transition in band 1.

performed. Data were collected at five different target-to-degrader separations of 135, 210, 300, 590, and 3000 μm during the experiment. These distances were chosen to provide a large variation of intensities in both the fully-shifted and degraded components of the 384-keV transition, as required by the RDDS method [4,21].

Figure 3(a) shows the total proton-tagged Ring 2 γ-ray spectrum corresponding to all target-to-degrader distances, x, used throughout the experiment. All of the spectra shown in Fig. 3 have been Doppler corrected using $v/c = 0.038(2)$ so that the fully shifted components of the ^{113}Cs transitions lie at the correct energy. However, it should be noted that this backward-facing ring of detectors corresponds to a laboratory angle of $\theta = 134°$ and therefore, the degraded component of each transition lies at a higher energy than the fully-shifted component. Figures 3(b) to 3(e) show the variation of the 384-keV transition component intensities, I_s and I_d, as a function of distance and illustrate how the dominant component changes from degraded at 389 keV to fully shifted at 384 keV as the distance is increased from 135 μm [Fig. 3(b)] to 3000 μm [Fig. 3(e)].

The corresponding spectra for the higher-lying, $(15/2^+)$ to $(11/2^+)$ feeding transition, are shown in Figs. 3(f) and 3(g). These spectra show that the fully shifted 596-keV component contains the majority of the transition intensity at the 135-μm [Fig. 3(f)] and 210-μm distances [Fig. 3(g)] with negligible intensity in the degraded component at 604-keV, even at these shortest target-to-degrader distances. This balance of shifted and degraded component intensities indicates that the lifetime of the $(15/2^+)$ state is much shorter than that of the $(11/2^+)$ state. As a consequence of this, a full RDDS lifetime analysis for the $(15/2^+)$ state could not be performed with the target-degrader foil distances used in this experiment for the $(11/2^+)$ state.

For all of the spectra shown in Figs. 3(b) to 3(g), Gaussian fits were used to extract the intensities of the fully shifted (green or purple) and degraded (red or cyan) components of the 384-keV $(11/2^+)$ to $(7/2^+)$ and 596-keV $(15/2^+)$ to $(11/2^+)$ transitions. The centroids and widths of the fully shifted 384-keV and 596-keV components were fixed using values deduced from a higher statistics summed spectrum of the two longest distances, 590 μm [Fig. 3(d)] and 3000 μm [Fig. 3(e)]. The degraded component of the $(11/2^+)$ to $(7/2^+)$ transition at 389 keV in this sum spectrum remained small and did not interfere with establishing the centroid and width of the fully shifted 384-keV component. Once the centroid and width of the fully shifted 384-keV peak were fixed, the 389-keV degraded component peak width and centroid could then be extracted from the sum of all target-to-degrader distances, see insert to Fig. 3(a). Table I summarizes the centroids and widths that were used to fit the intensities of the transitions shown in Fig. 3.

In contrast, for the 596-keV $(15/2^+)$ to $(11/2^+)$ transition, the small intensity of the degraded component at 604 keV meant that its centroid and width could not be fixed from the longest distance spectra in the same manner that was used for the 384-keV transition. Instead, the centroid of the degraded component of the $(15/2^+)$ to $(11/2^+)$ transition was calculated using the measured degraded $v/c = 0.018(2)$ to be 604.2 keV from its Doppler-shift relative to the fully shifted 596-keV
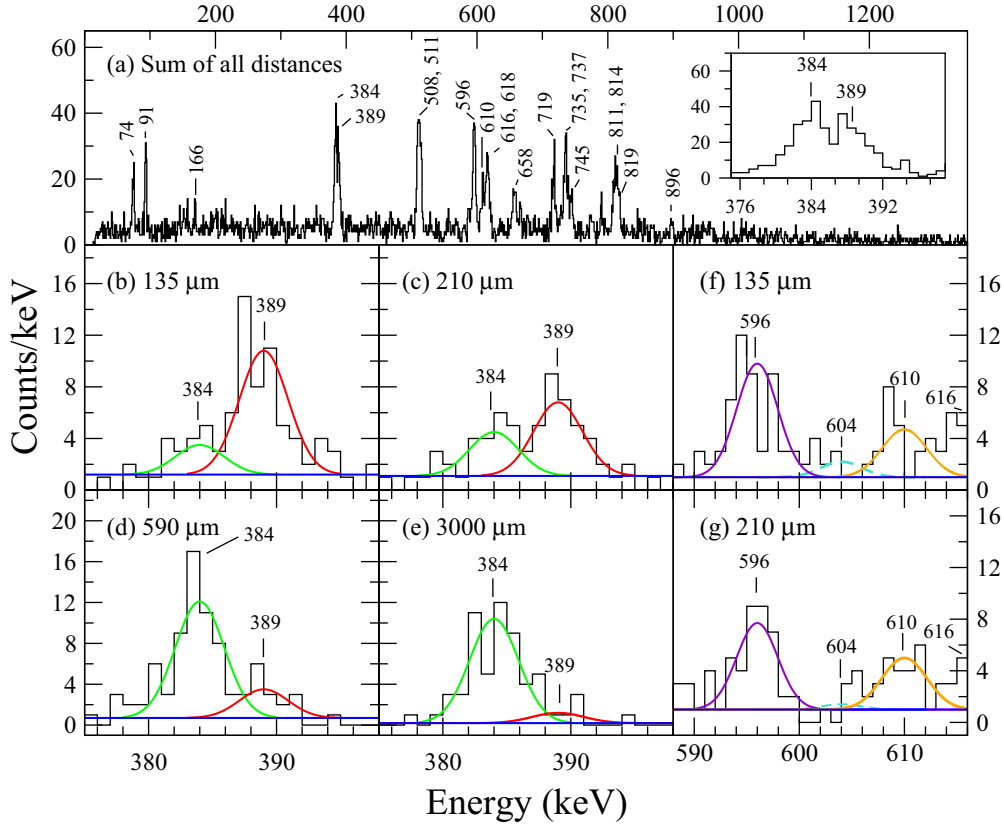
FIG. 3. ^{113}Cs proton-tagged fully Doppler-corrected Ring 2 ($\theta = 134°$) JUROGAM-II spectra. (a) A summed spectrum containing events from measurements made at all the distances. The inset is focused on the 384- and 389-keV peaks corresponding to the respective fully shifted and degraded components of the transition from the $(11/2^+)$ state. (b)–(g) Spectra corresponding to individual target-to-degrader distances, focused on the 384-keV [(b)–(e)] and 596-keV [(f) and (g)] γ-ray transitions from the $(11/2^+)$ and $(15/2^+)$ states in band 1. Gaussian fits to the fully shifted (red or purple) components and degraded (green or cyan) components are shown as well as the fully shifted component of the 610-keV transition from band 2 (orange).

peak. The peak width of the unobserved 604-keV component was calculated to be 0.3-keV wider than the 5-keV width of the observed 389-keV component from the increase in Doppler broadening expected at the higher 604-keV energy [22,33]. The widths and centroids of the fully shifted and degraded components of the $(15/2^+)$ to $(11/2^+)$ and $(11/2^+)$ to $(7/2^+)$ transitions were then fixed at the values shown in Table I across all distances for the RDDS [4] analysis. The intensities extracted from the fits in Figs. 3(b) to 3(g) were normalized to the total counts in the 957-keV ^{112}Te peak in a recoil-tagged Ring 2 γ-ray spectrum for each target-to-degrader distance. This normalization was applied to account for the differing data collection periods used for the different target-to-degrader

TABLE I. The widths and centroids used to fit the shifted and degraded components of the $(15/2^+) \rightarrow (11/2^+)$ and $(11/2^+) \rightarrow (7/2^+)$ transitions shown in Fig. 3. See text for details.

Transition	Component	Centroid (keV)	Width (keV)
$(11/2^+) \rightarrow (7/2^+)$	Fully-Shifted	384.1(4)	5.0(6)
$(11/2^+) \rightarrow (7/2^+)$	Degraded	388.9(3)	5.0(6)
$(15/2^+) \rightarrow (11/2^+)$	Fully-Shifted	596.3(5)	5.1(7)
$(15/2^+) \rightarrow (11/2^+)$	Degraded	604.2(9)	5.3(6)

distance settings. The 957-keV peak was chosen due to its high intensity, short lifetime and separation from other transitions in the recoil-tagged spectrum [34,35]. The normalized shifted and degraded component intensities of the $(15/2^+)$ to $(11/2^+)$ and $(11/2^+)$ to $(7/2^+)$ transitions are listed in Table II.

The lifetime of the $(11/2^+)$ state was determined using the differential decay curve method (DDCM) [21] using intensities listed in Table II according to

$$\tau_i(x) = -\frac{1}{\langle v \rangle} \frac{Q_{ij}^s(x) + \alpha(x)Q_{ih}^s(x)}{\frac{d}{dt}Q_{ij}^s(x)}. \tag{1}$$

The subscripts h,i, and j represent the $(15/2^+)$, $(11/2^+)$, and $(7/2^+)$ excited states, respectively. $Q_{ij}^s(x)$ are the normalized intensities of the fully shifted component of the 384-keV transition, $Q_{ih}^s(x)$ are the normalized intensities of the fully shifted component of the 596-keV transition. x represents the target-to-degrader distance, and the velocity of the fully shifted recoils, $\langle v \rangle = 0.038(2)c$. The term $\alpha(x)$ in Equation (1) reflects the difference in intensity between the feeding and depopulating transitions given by

$$\alpha(x) = \frac{Q_{ij}^s(x) + Q_{ij}^d(x)}{Q_{ih}^s(x) + Q_{ih}^d(x)}. \tag{2}$$

TABLE II. ^{113}Cs normalized fully-shifted, Q^s, and degraded, Q^d, component intensities of the 384-keV (ij) and 596-keV (ih) transitions in band 1 for each target-to-degrader distance, see text for details.

Target-to-degrader distance (μm)	Q_{ij}^s (Counts) 384-keV component	Q_{ij}^d (Counts) 389-keV component	Q_{ih}^s (Counts) 596-keV component	Q_{ih}^d (Counts) 604-keV component
135	13(5)	34(6)	43(7)	4(2)
210	18(6)	25(6)	35(6)	2(2)
300	24(7)	16(6)	36(7)	1(1)
590	46(7)	6(5)	37(6)	0(2)
3000	52(8)	5(5)	41(8)	4(2)

A value of $\alpha = 1.17(23)$ was determined from an average and standard deviation of the individual values of $\alpha(x)$ at each target-to-degrader distance. This indicates that there is likely some unobserved side-feeding populating the $(11/2^+)$ state, although the calculated value is consistent with the α value of 1.00(6) extracted from Ref. [11].

Figure 4 shows the DDCM fitting procedure used to extract the lifetime, τ_i, of the $(11/2^+)$ state based on Eq. (1) [21]. Figure 4(b) shows a piece-wise second-order polynomial fit to the variation of the normalized intensity, Q_{ij}^s, of the fully shifted component of the 384-keV transition as a function of target-to-degrader distance. Figure 4(c) shows the difference in fully shifted intensity as a function of distance, x, between the $(11/2^+)$ component and the $(15/2^+)$ component multiplied by the side-feeding parameter α. In the DDCM procedure, the

FIG. 4. Lifetime analysis for the $(11/2^+)$ state in ^{113}Cs based on the DDCM. (a) shows the 24(6)-ps lifetime of the $(11/2^+)$ state. This lifetime was calculated from a weighted average of the individual $\tau_i(x)$, corresponding to distances, x, of 135, 210, and 300 μm in the region of sensitivity. (b) shows the variation of the normalized intensity, Q_{ij}^s, of the fully shifted component of the 384-keV transition which depopulates the $(11/2^+)$ state as a function of distance. (c) shows the difference in fully shifted intensity as a function of distance between the $(11/2^+)$ component and the $(15/2^+)$ component multiplied by the side feeding parameter α. In (b) and (c), the piece-wise polynomial fit used to extract the lifetime in the DDCM are shown by the solid lines, as discussed in the text.

data shown in Figs. 4(b) and 4(c) are fitted simultaneously and the results of these fits are shown as solid lines in panels (b) and (c). The value of $\tau_i(x)$ was calculated at each distance within the "region of sensitivity" from a χ^2 minimization of the simultaneous fits. The region of sensitivity is defined as the range of target-to-degrader distances over which there is the largest change in intensity of the fully shifted component of the transition depopulating the level of interest and this is where the errors on the individual lifetimes are minimized [21]. A weighted average of the individual lifetimes $\tau_i(x)$ in the region of sensitivity was taken to provide a final value of $\tau_i = 24(6)$ ps for the lifetime of the $11/2^+$ state, see Fig. 4(a).

The full DDCM analysis could not be performed for the $(15/2^+)$ to $(11/2^+)$ transition, as the intensity of the 596-keV shifted component did not vary at the target-to-degrader distances optimized for the lifetime of the $(11/2^+)$ state in this experiment. However, the lifetime of the $(15/2^+)$ state has instead been estimated from the shifted and degraded component intensities of the $(15/2^+)$ to $(11/2^+)$ 596-keV transition from the shortest target-to-degrader distance, 135 μm. This was the shortest distance where some sensitivity to the lifetime of the $(15/2^+)$ state and a nonzero value for the number of counts in the degraded peak was observed (see Table II). Using this value, the lifetime of the $(15/2^+)$ state was estimated under the assumption that the $(19/2^+)$ state has a significantly shorter lifetime than the $(15/2^+)$ state and that no side-feeding was present. In particular an upper limit of $\tau_h < 5$ ps for the $(15/2^+)$ state lifetime was calculated according to

$$Q_{ih}^d = \left(Q_{ih}^s + Q_{ih}^d\right) \exp\left[-\frac{x}{v\tau_h}\right], \qquad (3)$$

using the data in Table II. Any lifetime value greater than this for the $(15/2^+)$ state would have been revealed by the observation of statistically significant nonzero counts in the 604-keV degraded component, Q_{ih}^d, at the larger target-to-degrader distances. Table II shows that this is not the case.

IV. DISCUSSION

In order to determine the magnitude of the deformation of the proton-emitting state in ^{113}Cs from the experimental results, theoretical quasiparticle model calculations have been performed using a deformed mean-field Woods-Saxon potential with spin-orbit interaction as discussed in Refs. [17,18]. In the present work, the theoretical calculations were based on the same approach with some additional improvements. In particular, these calculations were extended
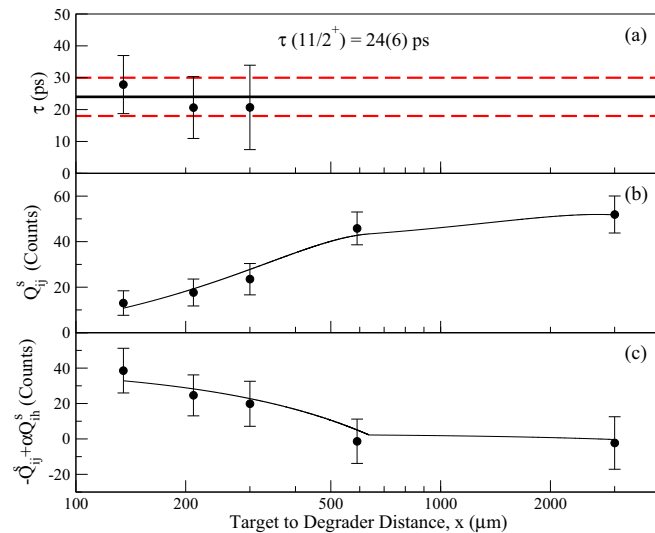
to allow for nonadiabatic cases where the core in the model is allowed to be less rigid. This is of particular use where nonrotational level schemes or components are experimentally established in the daughter nucleus [6]. In the current ^{113}Cs calculations, the experimental rotational spectrum of ^{112}Xe [36] was used as the core. Wave functions extracted from this model were then fixed and used consistently in both proton emission codes based on the approaches discussed in Ref. [18] and standard electromagnetic transition-rate calculations based on Refs. [37,38]. In this way, the half-lives for both proton emission and electromagnetic decays were predicted using a common set of wave functions.

1. Predicted excitation energies of the states

Figure 5 shows the predictions from the nonadiabatic quasiparticle model for the excitation energy of the states in Band 1 of ^{113}Cs (dashed lines) as a function of quadrupole deformation. Also shown are the experimental values (solid lines) from Ref. [11]. In the figure, the energies of the states have been plotted relative to the excitation energy of the $3/2^+$ state in Band 1 which is predicted to be the lowest state in energy for moderate deformations, $\beta_2 > 0.2$. Such deformation is consistent with both the previous predictions of Möller and Nix [15] and the single-particle decay width in the deformed Woods-Saxon calculations of Maglione *et al.* [16]. The excitation energies calculated from the nonadiabatic quasiparticle model in this work are in reasonable agreement with the experimental values, see Fig. 5. The predicted excitation energy of the $7/2^+$ state in Band 1 intersects the experimental value at a deformation of $\beta_2 = 0.24$. This deformation is consistent with the deformation of the $(3/2^+)$ state from Maglione *et al.* and also that of Möller and Nix discussed above. At higher angular momentum in Band 1, the quadrupole deformation predicted from the intersection of the experimental and theoretical lines appears to decrease. Figure 5 shows that the theoretical values only overlap with
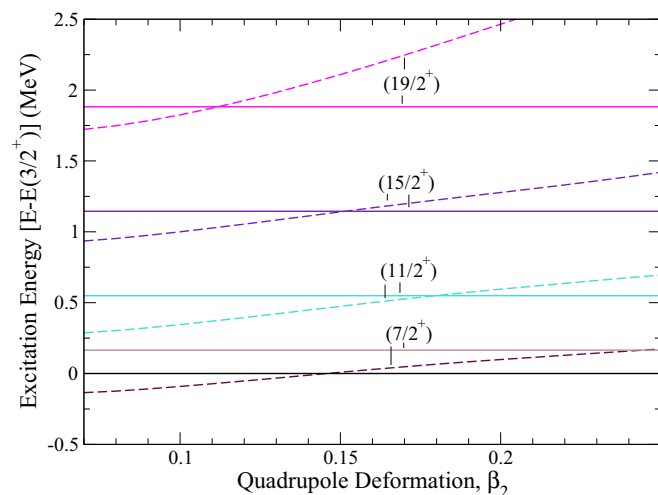
the experimental values with a lower deformation $\beta_2 = 0.18$ for the $(11/2^+)$ state and at $\beta_2 = 0.15$ for the $(15/2^+)$ state. This apparent reduction in deformation may, however, be reconciled from the aligned angular momentum plots for ^{113}Cs shown in Ref. [11]. At rotational frequencies of 0.37 MeV, the $(19/2^+)$ state was shown to already be influenced by the back-bending process and therefore, may no longer correspond to the more pure Band 1 configuration of the lower-spin $(3/2^+)$, $(7/2^+)$, and $(11/2^+)$ states calculated in the model. Such behavior may have lowered the experimental energy of the states (solid lines) relative to the theoretical (dashed) lines shown in Fig. 5, leading to an artificially reduced intersection at smaller deformation for the higher-spin states in Band 1.

With this reasonable agreement of the experimental excitation energy of the states with those predicted from the nonadiabatic quasiparticle model, the wave functions extracted from the model for the $(11/2^+)$ and $(15/2^+)$ states were then used to independently extract the γ-ray and proton-emission transition rates as a function of quadrupole deformation parameter.

2. Predicted B(E2) transition rates

Figures 6(a) and 6(b) show the predicted results of a standard electromagnetic reduced transition probability $B(E2)$ calculation [37,38] for the lifetimes of the $(11/2^+)$ and $(15/2^+)$ states in ^{113}Cs as a function of β_2 deformation, respectively. The calculations were based on the wave functions extracted from the nonadiabatic quasiparticle model calculation for the $(11/2^+)$ and $(15/2^+)$ states of ^{113}Cs. Also shown in Fig. 6(a) is the 24(6) ps lifetime for the $(11/2^+)$ state from the
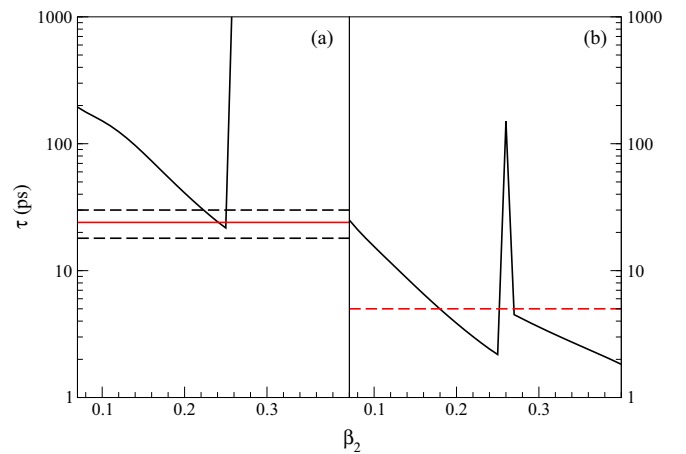

FIG. 6. Predicted excited-state lifetimes (a) $(11/2^+)$ and (b) $(15/2^+)$ as a function of quadrupole deformation in ^{113}Cs employing the quasiparticle wave functions that have been used to calculate the proton-emission half-life in Fig. 7 (see later). The experimental lifetime of the $(11/2^+)$ state and its uncertainty are denoted by the red and dashed lines in (a). The $\tau < 5$ ps limit for the $(15/2^+)$ state is denoted by the dashed line in (b), as discussed in the text. At deformations $\beta_2 > 0.25$ in the calculation, Band 1 is crossed by another configuration based on the [404]9/2 level, beyond which the lifetime is no longer reflective of the underlying configuration of Band 1.
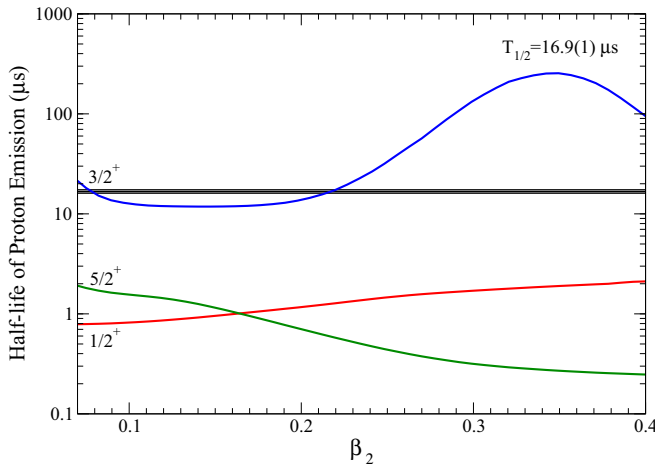

FIG. 5. Relative excitation energy of the states in Band 1 of ^{113}Cs as a function of quadrupole deformation. Solid lines represent the experimental values and dashed lines the theoretical predictions.

FIG. 7. Theoretical proton emission half-life as a function of quadrupole deformation for the low-spin states in ^{113}Cs using the non-adiabatic quasiparticle wave functions [17]. Also shown is the 16.9(1)-μs experimental value from this work which only overlaps with the calculated half-life of the $(3/2^+)$ state.

experimental DDCM analysis by the red and black dashed lines. From Fig. 6(a), it can be seen that the theoretical lifetime for the $(11/2^+)$ state is only consistent with the experimental $\tau = 24(6)$-ps RDDS experimental lifetime, deduced in this work for a quadrupole deformation parameter, $\beta_2 \sim 0.22$–0.25. In agreement with the analysis of the $(11/2^+)$ state, Fig. 6(b) shows the experimental $\tau < 5$ ps limit on the $(15/2^+)$ state estimated using the 4(2) counts in the 596-keV transition degraded component at the 135-μm distance shown in Table I. In Fig. 6, the theoretical values are only seen to overlap with this < 5 ps experimental limit for a quadrupole deformation $\beta_2 > 0.19$. At deformations $\beta_2 > 0.25$ in the calculation, Band 1 is crossed by another configuration based on the [404]9/2 level, beyond which the lifetime is no longer reflective of the underlying configuration of Band 1.

3. Predicted proton-emission transition rates

Using the same nonadiabatic quasiparticle model wave functions that were employed for the γ-ray transition rates discussed above, the lifetimes for proton emission have been calculated as a function of quadrupole deformation for the $1/2^+$, $3/2^+$, and $5/2^+$ states below the $(11/2^+)$ state [16]. Figure 7 shows the results of these calculations, along with the experimental half-life extracted in this work, 16.9(1) μs (solid black line). Agreement between the theoretical and experimental proton emission half-life is found for the $3/2^+$ state at deformation $\beta_2 = 0.08$ and also at $\beta_2 = 0.22$. The smaller β_2 value of 0.08 is discounted as a solution as it does not agree with the predicted deformations from neither the excitation energies of the states of Band 1, shown in Fig. 5, nor with the deformation predicted from the lifetime of the $(11/2^+)$

TABLE III. A summary of the deformation estimates for the $(11/2^+)$, $(15/2^+)$, and $(3/2^+)$ states from the various methods used in this work.

State	Result from	β_2
$(11/2^+)$	Excitation energy	~ 0.18
$(11/2^+)$	Lifetime measurement	0.22–0.26
$(15/2^+)$	Excitation energy	~ 0.15
$(15/2^+)$	Lifetime measurement	> 0.19
$(3/2^+)$	Proton emission lifetime	~ 0.22

or $(15/2^+)$ states discussed above. The higher $\beta_2 = 0.22$ value is however, in good agreement with the deformations extracted from the electromagnetic transition rates and also from the excitation energies of the states.

In order to deduce the most consistent deformation from the present work, the results from the various methods were used to extract deformations for the $(11/2^+)$, $(15/2^+)$, and $(3/2^+)$ states in ^{113}Cs, as summarized in Table III.

From Table III it can be seen that for the $(11/2^+)$ state, the range of deformations, from the excitation-energy calculation and the $B(E2)$ calculation, gives an average and standard deviation, $\beta_2 = 0.22(6)$. This deformation and its uncertainty is dominated by the $B(E2)$ calculation which is the most sensitive part our method. The deformation limit extracted for the $(15/2^+)$ state lifetime limit is in agreement, giving $\beta_2 > 0.19$. Finally, the proton lifetime measurement for the $(3/2^+)$ state in this work is also consistent with this deformation $\beta_2 = 0.22(6)$.

In summary in this work, the lifetime of the $(11/2^+)$ state in ^{113}Cs has been measured for the first time to be $\tau = 24(6)$ ps. A limit of $\tau < 5$ ps was also placed on the higher lying $(15/2^+)$ state. The half-life of the proton emitting $(3/2^+)$ state has been remeasured to be 16.9(1) μs and is found to be in agreement with the previously accepted value. In order to interpret these results, wave functions from a nonadiabatic quasiparticle model have been used to calculate both proton-emission and γ-ray transition rates for ^{113}Cs. The only deformation which matches the experimental lifetime and excitation energy of the $(11/2^+)$ and $(15/2^+)$ states, and the proton-emission lifetime is found to be $\beta_2 = 0.22(6)$. This deformation is consistent with the earlier predictions for ^{113}Cs [14–16] but is now, for the first time, more firmly based on an approach supported by an experimental RDDS lifetime measurement.

[1] P. J. Woods and C. N. Davids, Annu. Rev. Nucl. Part. Sci. **47**, 541 (1997).

[2] M. Pfutzner, M. Karny, L. V. Grigorenko, and K. Riisager, Rev. Mod. Phys. **84**, 567 (2012).

[3] M. J. Taylor *et al.*, Nucl. Instrum. Methods Phys. Res. A **707**, 143 (2013).

[4] A. Dewald, O. Müller, and P. Petkov, Prog. Part. Nucl. Phys. **67**, 786 (2012).

[5] M. G. Procter *et al.*, Phys. Lett. B **704**, 118 (2011).

[6] M. G. Procter *et al.*, Phys. Lett. B **725**, 79 (2013).

[7] T. Faestermann, A. Gillitzer, K. Hartel, P. Kienle, and E. Nolte, Phys. Lett. B **137**, 23 (1984).

[8] A. Gillitzer, T. Faestermann, K. Hartel, P. Kienle, and E. Nolte, Z. Phys. A At. Nucl. **326**, 107 (1987).

[9] R. D. Page *et al.*, Phys. Rev. Lett. **72**, 1798 (1994).

[10] J. C. Batchelder *et al.*, Phys. Rev. C **57**, R1042 (1998).

[11] P. T. Wady *et al.*, Phys. Lett. B **740**, 243 (2015).

[12] S. Åberg, P. B. Semmes, and W. Nazarewicz, Phys. Rev. C **56**, 1762 (1997).

[13] S. Åberg, P. B. Semmes, and W. Nazarewicz, Phys. Rev. C **58**, 3011 (1998).

[14] V. P. Bugrov and S. G. Kadmensky, Sov. J. Phys. **49**, 967 (1989).

[15] P. Moller, J. R. Nix, W. D. Myers, and W. J. Swiatecki, At. Data Nucl. Data Tables **59**, 185 (1995).

[16] E. Maglione, L. S. Ferreira, and R. J. Liotta, Phys. Rev. Lett. **81**, 538 (1998).

[17] L. S. Ferreira, M. Costa Lopes, and E. Maglione, Int. J. Mod. Phys. E **15**, 1789 (2006).

[18] G. Fiorin, E. Maglione, and L. S. Ferreira, Phys. Rev. C **67**, 054302 (2003).

[19] M. J. Taylor *et al.*, Phys. Rev. C **91**, 044322 (2015).

[20] C. H. Yu *et al.*, AIP Conf. Proc. **681**, 172 (2003).

[21] A. Dewald, S. Harissopulos, and P. Brentano, Z. Phys. A At. Nucl. **334**, 163 (1989).

[22] C. W. Beausang *et al.*, Nucl. Instrum. Methods Phys. Res. A **313**, 37 (1992).

[23] G. Duchêne *et al.*, Nucl. Instrum. Methods Phys. Res. A **432**, 90 (1999).

[24] C. W. Beausang and J. Simpson, J. Phys. G: Nucl. Part. Phys. **22**, 527 (1996).

[25] M. Leino *et al.*, Nucl. Instrum. Methods Phys. Res. B **99**, 653 (1995).

[26] R. D. Page *et al.*, Nucl. Instrum. Methods Phys. Res. B **204**, 634 (2003).

[27] I. H. Lazarus *et al.*, IEEE Trans. Nucl. Sci. **48**, 567 (2001).

[28] P. Rahkila, Nucl. Instrum. Methods Phys. Res. A **595**, 637 (2008).

[29] E. S. Paul *et al.*, Phys. Rev. C **51**, 78 (1995).

[30] P. T. Wady *et al.*, Phys. Rev. C **85**, 034329 (2012).

[31] P. J. Sellin *et al.*, Phys. Rev. C **47**, 1933 (1993).

[32] M. G. Procter *et al.*, Phys. Rev. C **87**, 014308 (2013).

[33] S. Shepherd *et al.*, Nucl. Instrum. Methods Phys. Res. A **434**, 373 (1999).

[34] M. Doncel *et al.*, Phys. Rev. C **91**, 061304(R) (2015).

[35] E. S. Paul *et al.*, Phys. Rev. C **75**, 014308 (2007).

[36] J. F. Smith *et al.*, Phys. Lett. B **523**, 13 (2001).

[37] R. Popli, J. A. Grau, S. I. Popik, L. E. Samuelson, F. A. Rickey, and P. C. Simms, Phys. Rev. C **20**, 1350 (1979).

[38] A. Bohr and B. R. Mottelson, *Nuclear Structure* (W. A. Benjamin, Inc., New York, 1975), Vol. I, p. 332.